

1 **DOI: <https://doi.org/10.47391/JPMA.1203>**

2
3 **Anatomic study of carpal tunnel in adults using monoenergetic**
4 **reconstruction of dual-energy computed tomography**

5
6 **Heng Zhao¹, Fei Peng², De-Qiu Tang³, Jin-Cai Liu⁴, Hao Lei⁵, Qiang Liu⁶,**
7 **Fang Wang⁷, Qiu-Ping Ren⁸, Jiao Yang Li⁹, Feng-zhe Wang¹⁰, Zhao Lu¹¹,**
8 **Shi Nong Pan¹²**

9 **1,6,11,12** Department of Radiology, Shengjing Hospital of China Medical University,
10 Shenyang, China; **2,3,4,5,7,8** Department of Radiology, The First Affiliated Hospital of
11 University of South China, Hengyang, Hunan, China; **9** Department of Metabolism and
12 Endocrinology, The First Affiliated Hospital of University of South China, Hengyang, Hunan,
13 China; **10** Department of Radiology, The 4th people Hospital of Shenyang, Shenyang, China

14 **Correspondence:** Shi Nong Pan. **Email:** cjr.panshinong@vip.163.com

15
16 **Abstract**

17 **Purpose:** To seek optimal keV settings for imaging carpal tunnel in adults by
18 dual-energy computed tomography (DECT) monoenergetic technique; to
19 describe anatomic characteristics of carpal tunnel and to observe correlation
20 between carpal bony and soft tissue structures.

21 **Methods:** DECT images of 20 wrists (11 left and 9 right wrists; 14 men, mean
22 age 26.93 ± 1.38 years, range 23 to 28, and 6 women, mean age 24.17 ± 0.98
23 years, range 23 to 26) were evaluated. Monoenergetic images were
24 reconstructed at 42, 62, 82, 102, 122, and 142 keV. Image quality was assessed
25 along a 5-point Likert scale, and the highest-quality images were chosen for
26 quantitative analysis. Two musculoskeletal radiologists performed both analyses
27 independently.

28 **Results:** The optimal energy spectrum with the best contrast-to-noise ratio

29 (CNR) for monoenergetic images were at 62 keV (19 wrists, 95%) and 61 keV
30 (1 wrist, 5%). There was substantial interobserver agreement between the
31 readers in the 5-point Likert scale analysis of image quality ($\kappa = 0.793$). Bland-
32 Altman plots also indicated good agreement between observers in quantitative
33 analysis. Intra-category 1 and 2 correlation was mostly discovered at hamate
34 hook level and middle level of pisiform ($P < 0.05$), while bony and soft tissue
35 structures partly reached correlation ($P < 0.05$).

36 **Conclusion:** The optimal energy spectrum for monoenergetic DECT imaging of
37 carpal tunnel structures was 62 keV. DECT monoenergetic imaging could
38 predict changes in soft tissue structures and demonstrate carpal tunnel anatomic
39 structures.

40 **Keywords:** DECT, monoenergetic, keV, carpal tunnel, anatomy.

41

42 **Introduction**

43 The anatomy of carpal tunnel is complex, and inflammation of internal
44 structures can easily elevate intra-carpal tunnel pressure, leading to entrapment
45 of median nerve (MN) and development of carpal tunnel syndrome (CTS). CTS
46 causes pain and paresthesias, and severe cases may result in deformity and
47 disability of upper extremity.¹

48 Magnetic resonance imaging (MRI) has demonstrated superiority in imaging of
49 soft tissues and bony structures of carpal tunnel, and provides high-quality
50 images,² but clinical application of MRI might be limited because of time
51 constraints or contraindications. Ultrasound is an effective, noninvasive, non-
52 radioactive method of examination that is comparable to MRI in terms of
53 resolution of soft tissues of carpal tunnel region.³ However, ultrasound cannot
54 penetrate bones or depict lesions of deep bony tissues, thus limiting overall
55 diagnostic efficacy for diseases of musculoskeletal system. Traditional
56 computed tomography (CT) is well known for advantages such as rapid
57 scanning and few contraindications, and single energy CT (SECT) has proven

58 incomparable in evaluation of bony structures of carpal tunnel. SECT readily
59 displays bony abnormalities and conditions associated with bony deformities
60 that occupy carpal tunnel space. SECT can accurately predict bony etiology,
61 location, and extent of carpal tunnel stenosis through thin axial images,
62 multiplane reformation, and 3D reconstruction.⁴ However, the resolution of
63 SECT for display of soft tissues is poor, and it is usually only applicable when
64 bony structure damage or injury is suspected.⁵

65 DECT has inherited the advantages of SECT for display of bony structures, and
66 it offers better resolution of soft tissues, allowing for better visualization of soft
67 tissue structures such as tendons and ligaments.⁶ DECT imaging incorporates
68 information from low- and high-energy data that are synchronously acquired
69 during a single scan,⁷ and DECT workstation offers several post-processing
70 techniques, including production of virtual monoenergetic images that can be
71 generated at any desired energy level; the CNR of these virtual images can be
72 optimized for significantly improved image quality.⁸ However, as yet, there are
73 no published reports regarding application of monoenergetic DECT imaging for
74 carpal tunnel.

75 Our purpose was to assess monoenergetic DECT imaging of carpal tunnel in
76 adults and seek the optimal energy spectrum, to further understand anatomic
77 characteristics of internal carpal structures and the correlation between carpal
78 bony and soft tissue elements.

79

80 **Materials and Methods**

81 This study gained the approval from the Medical Ethic Committee of University
82 of South China. Between January 2016 and February 2017, we sequentially
83 chose 24 young adult patients (range 23 to 28 years) with acute single wrist
84 trauma and suspicion of bony injury on initial CT scan, after gaining informed
85 consent from the patients, DECT was performed on normal contralateral
86 wrist(uninjured) for comparison, so as to judge the suspected bony injury.

87 Hence we obtained 24 normal (uninjured) adult wrists and included them for
88 initial study. After monoenergetic reconstruction of DECT data, wrists with
89 bifid median nerve (MN) (n=2) and poor-quality images (n=2) were excluded.
90 Thus, final analysis included 20 normal(uninjured) wrists (11 left wrists and 9
91 right wrists) from 14 men (average age 26.93 ± 1.38 years; range 23 to 28 years)
92 and 6 women (average age 24.17 ± 0.98 years; range 23 to 26 years) (Figure 1).
93 Scanning was performed with a 256 row dual source CT (Somatom Definition;
94 Siemens, Germany). A dual source mode was applied to CT scanning
95 (collimation, 64×0.6 mm; pitch, 0.7; rotation time, 0.33 sec) with patients prone
96 and wrists in resting position. The tube voltages were set as 80 kVp (tube A)
97 and 140 kVp (tube B). The predefined tube current-time was configured for 2:1
98 ratio, with effective mAs of tube A and tube B were 220 and 110, respectively.
99 Each DECT scanning generated three different sets of images, included 80kVp,
100 140 kVp and weighted average (120 kVp). Three corresponding sets of
101 transverse images with 0.6 mm section thickness were reconstructed.
102 The acquired data were post-processed using dedicated dual-energy
103 monoenergetic software on a Siemens workstation (SyngoMMWP VE40B).
104 First, we outlined a region of interest (ROI) in the soft tissue structure area of
105 carpal tunnel, after which, through a monoenergetic technique, corresponding
106 optimal spectrum with the best CNR was obtained. Monoenergetic images were
107 then reconstructed respectively at six energy values separated by 20 keV
108 increments.¹⁰
109 Two musculoskeletal system radiologists (with 4 and 16 years of experience,
110 respectively) evaluated the image quality independently. We scored image
111 quality along Likert Scale, with 1, poor; 2, adequate; 3, average; 4, good; and 5,
112 excellent.¹¹
113 We chose the highest quality (Likert score 5) images for objective analysis. Four
114 levels of the wrist were identified. The first level was proximal section at distal
115 radioulnar joint was seen. The second level was located in middle of pisiform,

116 which represented entrance of carpal tunnel. The third level was situated at
117 hamate hook (middle part of carpal tunnel). The fourth level was placed at the
118 point where proximal metacarpal bones became visible. The measurements are
119 shown in Fig 2. The same two radiologists measured the image data
120 independently.

121 Taking optimal energy spectrum settings ratio $\geq 70\%$ as basic requirement, 95%
122 of the 62 keV settings ratio as research data, power $(1-\beta)$ set at 0.80 and $\alpha =$
123 0.05 (one side). Sample size was calculated by the formula $n = (\mu_\alpha + \mu_\beta / \delta)^2 \pi_0 (1 - \pi_0)$.
124 ⁹ In total, minimum sample size was 20. In subjective analysis of Likert Scale
125 images, Cohen's kappa (κ) was used to verify consistency between the two
126 observers. In objective image analysis, Bland-Altman plots were presented to
127 demonstrate the level of agreement between two independent readers. The
128 numerical values measured at four levels were analyzed by using one-way
129 ANOVA and Pearson correlation. The difference was statistically significant at
130 $P < 0.05$. SPSS Version 17.0 and Medcalc Version 17.8 were used for statistical
131 analysis.

132

133 **Results**

134 In 20 wrists, the optimal energy spectrum with the best CNR on monoenergetic
135 images was 62keV (19 wrists, 95%); one wrist showed the best quality at 61keV.
136 All monoenergetic images were reconstructed at 42, 62, 82, 102, 122, and 142
137 keV (Fig 3), and Likert scores confirmed that reconstructions at 62 keV had
138 highest quality. The overall interobserver agreement for Likert scale grading
139 was substantial ($\kappa = 0.793$).

140 The means \pm standard deviations (SD) of cross-sectional area (CSA) of carpal
141 tunnel, CSA of MN, the long axis and short axis of MN, swelling ratio (CSA of
142 MN at the pisiform bone level/CSA of MN at distal radioulnar joint level), and
143 flattening ratio of MN (long axis/short axis); CT units of MN, flexor
144 retinaculum (FR), and tendon; and bowing of transverse carpal ligament (TCL),

145 length of the capitate, carpal arch width (CAW), carpal arch length (CAL),
146 carpal arch area (CAA), and width and depth of carpal bony structures are
147 shown in Table 1. Bland-Altman plots for the measurements showed good
148 agreement between two independent observers (Fig 4).

149 The hamate hook level was chosen as the focal point for statistical analysis ($*P$
150 < 0.05 , $**P < 0.01$, $***P < 0.001$). We classified carpal tunnel
151 structures according to anatomic tendency, with category 1 showing steep
152 changes (V- or inverted V-shape) and category 2 increasing or decreasing
153 gradually (Fig 5).

154 Correlation between carpal tunnel structures in category 1 (Table 2) and
155 category 2 (Table 3) was examined at four levels. In both categories, intra-
156 category correlation was mostly found at hamate hook level and middle level of
157 pisiform, followed by the level of proximal metacarpal bone. At the distal
158 radioulnar joint level, intra-category correlation was not obvious in either
159 category. Correlation analysis between carpal bony and soft tissue structures at
160 three levels is shown in Table 4. The greatest correlation between the widths of
161 bony and soft tissue structures was found at hamate hook level and proximal
162 metacarpal bones level, and the greatest correlation in the depth of carpal tunnel
163 bony and soft tissue structures was found at hamate hook level and middle level
164 of pisiform. Taken together, the bony and soft tissue structures of carpal tunnel
165 reached the most obvious correlation at hamate hook level. Meanwhile, CSA of
166 the carpal tunnel was correlated with width and depth of the bony structures at
167 three levels.

168

169 **Discussion**

170 Significant improvements in image quality have been reported with
171 monoenergetic techniques in a variety of tissues and organs, and corresponding
172 optimal energy spectrum are also reported.^{12,13} We hypothesized that this

173 technique would also be useful for the structures of carpal tunnel. Images that
174 were reconstructed at 62 keV had good inter-observer agreement in analysis,
175 and we, therefore, recommend 62 keV as the optimal energy spectrum for
176 monoenergetic DECT imaging of structures of carpal tunnel.

177 The MN is often compressed at hamate hook level due to regional stenosis, firm
178 structure, and high pressure, and level of hamate hook has been a focal point in
179 the study of CTS.¹⁴ Thus, we chose this level as the basis for our statistical
180 analysis.

181 The CSA of carpal tunnel was lowest at the level of hamate hook, and this
182 finding was consistent with previous reports. Gabra et al found the CSA of
183 carpal tunnel at hamate hook level was 20% less than that of other levels.¹⁵ The
184 anatomic tendency at CSA in our study was also consistent with the findings of
185 Oge et al, who reported a similar anatomic tendency of CSA of carpal tunnel at
186 MRI.¹⁶ MRI has consistently shown that the smallest CSA of carpal tunnel is
187 found at hamate hook level,¹⁶ and it is thought that CSA at hamate hook level is
188 more susceptible to pressure changes in carpal tunnel,¹⁷ thus, this level should
189 be a focal point in imaging observation.

190 The FR can be divided into three successive segments: proximal slender
191 segment, central firm segment and distal thin segment.⁵ The FR was thickest at
192 hamate hook level in a cadaver study,¹⁸ and in our study, the highest CT number
193 for FR was measured at hamate hook level, indicating that FR reached its
194 greatest density at this level. We thought this might be because intra-tunnel
195 tissues are more protected at the level of hamate hook.

196 Regarding MN, there are conflicting results as to CSA, as demonstrated by
197 inconsistency in anatomic tendency and in the reporting of CSA at different
198 levels. With respect to anatomic tendency, Monagle found that the change was
199 not obvious,¹⁹ while several other authors reported that MN assumed a "head-
200 neck-body" morphology as it passed through carpal tunnel, with "neck" at
201 hamate hook,²⁰ and still others argued that the tendency was more N-shaped and

202 that the narrowest region was at the level of distal radioulnar joint.²¹ In terms of
203 quantitative assessments, the reported mean values of CSA of MN range from
204 8.6 mm² to 22.7 mm².²¹⁻²³ One reason for this wide variation might be that the
205 small cross section creates difficulty in establishing optimal ROIs for
206 measurements. Furthermore, the measurements could be affected by sample
207 sizes and by the mode of imaging. In our study, anatomic tendency of MN
208 resembled an inverted V, and the max CSA was at the level of hamate hook.
209 Deniz et al considered CT inadequate for visualizing MN,⁴ and although
210 monoenergetic imaging might enhance visibility of MN, cross-sectional
211 imaging of the nerve by DECT might still be insufficient.

212 The anatomic tendency of flattening ratio of MN was increased gradually. MRI
213 findings have described flattening ratio of MN at each levels as: hamate hook >
214 pisiform > distal radioulnar joint,¹⁹ which is also approximately consistent with
215 our findings. Collectively, the anatomic tendency of category 1 and 2 in our
216 study was similar to that of most previous research. Thus, we believe DECT has
217 a degree of potential for resolution of soft tissues of carpal tunnel.

218 In patients with CTS, morphological changes of carpal tunnel often occur at
219 hamate hook level and middle level of pisiform bone.¹⁴ Our finding that intra-
220 category 1 and 2 correlation occurred mostly at hamate hook level and middle
221 level of pisiform, suggested a clear correlation among morphological changes of
222 intra-carpal structures at the two levels.

223 The morphology of carpal tunnel largely depends on carpal bony structures, and
224 movement of carpal bones could partly change intra-carpal tunnel structures.²⁴

225 Displaced fractures and malalignment or deformity of carpal bones would
226 change carpal tunnel volume and tend to elevate intra-carpal tunnel pressure,
227 leading to entrapment of MN and contributing to CTS, which further
228 demonstrated interplay between carpal bony and soft tissue structures.²⁵

229 Similarly, in cadaver specimens, carpal tunnel pressure increased with
230 narrowing of carpal bony structures, while bowing of TCL and CSA of carpal

231 tunnel at hamate hook level were forced to increase in order to accommodate
232 the greater pressure, which again demonstrated the relationship between carpal
233 bony structures and potential ability of carpal tunnel to expand under pressure.¹⁷
234 In our study, carpal tunnel bony structures correlated with soft tissue structures,
235 especially at hamate hook level. Furthermore, we found that CSA of carpal
236 structures were all correlated with width and depth of bony structures at three
237 levels. The CSA of carpal tunnel have been reported in association with CTS.¹⁶
238 Hence, we surmised that the changes of carpal bony structures might be helpful
239 in the diagnosis of CTS.

240 There were several limitations in this study. First, we did not use MRI images
241 for reference, because our purpose was to study the anatomic tendency of adult
242 carpal tunnel structures on DECT, rather than to verify the diagnostic efficiency
243 of DECT. Second, all were young adults, and did not take into account
244 variations in age, gender, height, weight, or handedness; besides, the study
245 sample size was small. Third, although the total radiation dose of DECT is
246 below the accepted threshold, it is still higher than that of SECT.

247

248 **Conclusion**

249 The optimal energy spectrum for imaging carpal tunnel structures by
250 monoenergetic DECT was 62 keV. DECT permits a degree of visualization of
251 soft tissues in carpal tunnel and was able to demonstrate the anatomic tendency
252 of carpal tunnel structures. Carpal bony structures correlated with carpal soft
253 tissue, and especially correlated with the CSA of carpal tunnel. As DECT
254 technology evolves, we believe it has good prospects in clinical evaluation.

255

256 **Disclaimer:** None to declare

257 **Conflict of Interest:** None to declare

258 **Funding Disclosure:** This work was funded by the National Key Research and
259 Development Program of China (Grant No. 2016YFC0107102 (S. P.)), the

260 National Natural Science Foundation of China (Grant No. 81271538 (S. P.)),
261 Hunan Provincial Natural Science Foundation of China (Grant No.
262 2017JJ2225(J. L.)), Hunan Provincial Science and Technology Innovation
263 Program of China (Grant No. 2017SK50203 (H. Z.)). The funders had no role in
264 study design, data collection and analysis, decision to publish, or preparation of
265 the manuscript.

266

267 **References**

- 268 1. Festen-Schrier VJMM, Amadio PC. The biomechanics of subsynovial
269 connective tissue in health and its role in carpal tunnel syndrome. J
270 Electromyogr Kinesiol 2018;38:232-239.
- 271 2. Meraj S, Gyftopoulos S, Nellans K et al. MRI of the Extensor Tendons of
272 the Wrist. AJR Am J Roentgenol 2017; 209: 1093-1102.
- 273 3. Chen YT, Williams L, Zak MJ. Review of Ultrasonography in the
274 Diagnosis of Carpal Tunnel Syndrome and a Proposed Scanning Protocol. J
275 Ultrasound Med 2016; 35:2311-2324.
- 276 4. Deniz FE, Oksüz E, Sarikaya B et al. Comparison of the diagnostic utility
277 of electromyography, ultrasonography, computed tomography, and
278 magnetic resonance imaging in idiopathic carpal tunnel syndrome
279 determined by clinical findings. Neurosurgery 2012; 70:610-616.
- 280 5. Ghasemi-Rad M, Nosair E, Vegh A et al. A handy review of carpal tunnel
281 syndrome: From anatomy to diagnosis and treatment[J]. World J Radiol
282 2014; 6: 284-300.
- 283 6. Mallinson PI, Coupal TM, McLaughlin PD. et al. Dual-Energy CT for the
284 Musculoskeletal System. Radiology. 2016;281(3):690-707.
- 285 7. Kosmala A, Weng AM, Heidemeier A et al. Multiple Myeloma and Dual-
286 Energy CT: Diagnostic Accuracy of Virtual Noncalcium Technique for
287 Detection of Bone Marrow Infiltration of the Spine and Pelvis.
288 Radiology.2018; 286(1):205-213.

- 289 8. Schmoee J, Dirrichs T, Fehrenbacher K et al. Virtual Monoenergetic
290 Images (VMI+) in Dual-Source Dual-Energy CT Venography (DSDE-CTV)
291 of the Lower Extremity Prior to Coronary Artery Bypass Graft (CABG): A
292 Feasibility Study. *Acad Radiol*. 2019; S1076-6332(19)30558-6.
- 293 9. Sun ZQ. *Medical Statistics [M]*. Third Edition. Beijing: People's Medical
294 Publishing House, 2010.
- 295 10. Dong Y, Zheng S, Machida H et al. Differential diagnosis of osteoblastic
296 metastases from bone islands in patients with lung couldcer by single-
297 source dual-energy CT: advantages of spectral CT imaging. *Eur J Radiol*
298 2015; 84:901-907.
- 299 11. Linsen PV, Coenen A, Lubbers MM et al. Computed Tomography
300 Angiography with a 192-slice Dual-source Computed Tomography System:
301 Improvements in Image Quality and Radiation Dose. *J Clin Imaging* 2016;
302 6:44.
- 303 12. Wichmann JL, Noske EM, Kraft J, et al. Virtual monoenergetic dual-energy
304 computed tomography: optimization of kiloelectron volt settings in head
305 and neck couldcer. *Invest Radiol* 2014; 49:735–741.
- 306 13. Lenga L, Albrecht MH, Othman AE et al. Monoenergetic Dual-energy
307 Computed Tomographic Imaging: Cardiothoracic Applications. *J Thorac*
308 *Imaging* 2017; 32:151-158.
- 309 14. Goss BC, Agee JM. Dynamics of intracarpal tunnel pressure in patients
310 with carpal tunnel syndrome. *J Hand Surg Am* 2010; 35:197–206.
- 311 15. Gabra JN, Kim DH, Li ZM. Elliptical Morphology of the Carpal Tunnel
312 Cross Section. *Eur J Anat* 2015; 19:49-56.
- 313 16. Oge HK, Acu B, Gucer T. et al. Quantitative MRI analysis of idiopathic
314 carpal tunnel syndrome. *Turk Neurosurg* 2012; 22:763-768.
- 315 17. Li ZM, Masters TL, Mondello TA. Area and shape changes of the carpal
316 tunnel in response to tunnel pressure. *J Orthop Res* 2011; 29:1951-1956.
- 317 18. Nanno M, Sawaizumi T, Kodera N et al. Three-dimensional Analysis of the

- 318 Attachment and Path of the Transverse Carpal Ligament. J Nippon Med
319 Sch 2015; 82:130-135.
- 320 19. Monagle K, Dai G, Chu A. et al. Quantitative MR imaging of carpal tunnel
321 syndrome. AJR Am J Roentgenol 1999; 172:1581-1586.
- 322 20. Nakamichi KI, Tachibana S. Enlarged median nerve in idiopathic carpal
323 tunnel syndrome. Muscle Nerve 2000; 23:1713–1718.
- 324 21. Jarvik JG, Yuen E, Haynor DR et al. MR nerve imaging in a prospective
325 cohort of patients with suspected carpal tunnel syndrome. Neurology 2002;
326 58:1597-1602.
- 327 22. Yao L, Gai N. Median nerve cross-sectional area and MRI diffusion
328 characteristics: normative values at the carpal tunnel. Skeletal Radiol 2009;
329 38:355-361.
- 330 23. Cha JG, Han JK, Im SB et al. Median nerve T2 assessment in the wrist
331 joints: preliminary study in patients with carpal tunnel syndrome and
332 healthy volunteers. J Magn Reson Imaging 2014; 40:789-795.
- 333 24. Mogk Jp, Keir pJ. The effect of landmarks and bone motion on posture-
334 related changes in carpal tunnel volume. Clin Biomech (Bristol, Avon)
335 2009; 24:708-715.
- 336 25. Niver GE, Ilyas AM. Carpal tunnel syndrome after distal radius fracture.
337 Orthop Clin North Am 2012; 43:521-527.

338

339

340

341 **Table 1 The means \pm SD of carpal tunnel structures at four levels**

	The distal radioulnar joint	The middle of the pisiform bone	The hamate hook	The proximal metacarpal bones
CSA of carpal tunnel (mm ²)	150.71 \pm 37.35	142.06 \pm 33.24	119.80 \pm 21.28	146.79 \pm 23.83
CSA of MN (mm ²)	7.15 \pm 1.59	12.78 \pm 3.36	15.47 \pm 2.02	13.23 \pm 2.59
Long axis of MN (mm)	3.31 \pm 0.45	4.92 \pm 0.85	6.19 \pm 0.61	6.48 \pm 0.75
Short axis of MN (mm)	2.33 \pm 0.34	3.19 \pm 0.53	3.35 \pm 0.52	2.68 \pm 0.44
Flattening ratio of MN	1.42 \pm 0.15	1.59 \pm 0.44	1.92 \pm 0.41	2.57 \pm 0.60
CT unit of FR (HU)	-0.27 \pm 10.08	52.68 \pm 15.40	75.01 \pm 8.13	69.06 \pm 10.48
Width of carpal tunnel bony structure (mm)		31.45 \pm 3.22	23.06 \pm 2.27	36.98 \pm 3.88
Depth of carpal tunnel bony structure (mm)		11.50 \pm 1.34	10.35 \pm 0.85	8.06 \pm 0.57
CT unit of MN (HU)	43.00 \pm 7.47	52.98 \pm 6.27	51.45 \pm 7.77	52.34 \pm 4.04
CT unit of tendon (HU)	99.10 \pm 5.72	100.58 \pm 3.91	96.49 \pm 4.12	92.11 \pm 3.79

CAW (mm)		18.55 ± 1.61
CAL (mm)		19.84 ± 1.78
CAA (mm ²)		20.71 ± 2.59
Bowing of TCL (mm)		0.08 ± 0.92
Swelling ratio of MN	1.79 ± 0.39	
Length of the capitata (mm)		21.35 ± 1.29

342

343

344

345

Table 2 Correlation analysis among Category 1 values at four levels

346

	The distal radioulnar joint				The middle of pisiform bone				The hamate hook			
	CSA of MN	Short axis of MN	CSA of carpal tunnel	Width of bony structure	CSA of MN	Short axis of MN	CSA of carpal tunnel	Width of bony structure	CSA of MN	Short axis of MN	CSA of carpal tunnel	Width of bony structure
CSA of MN	1				1				1			
Short axis of MN	0.693**	1			0.809***	1			0.544*	1		
CSA of carpal tunnel	0.198	0.171	1		0.771***	0.696**	1		0.646**	0.408	1	
Width of bony structure	NA	NA	NA	1	0.365	0.268	0.769***	1	0.362	-0.251	0.499*	1

347

* $P < 0.05$, ** $P < 0.01$, *** $P < 0.001$; NA, not available

348

349

350

351

Table 3 Correlation analysis among Category 2 values at four levels

352

Flattening ratio of MN	The distal radioulnar joint			The middle of pisiform bone			The hamate hook			The proximal metacarpal bones	
	long axis of MN	Depth of bony structure	Flattening ratio of MN	long axis of MN	Depth of bony structure	Flattening ratio of MN	long axis of MN	Depth of bony structure	Flattening ratio of MN	long axis of MN	
1			1			1			1		
0.379	1		0.518*	1		0.629**	1		0.593**	1	
NA	NA	1	-0.515*	0.116	1	-0.461*	-0.166	1	0.383	0.434	

353

* $P < 0.05$, ** $P < 0.01$, *** $P < 0.001$; NA, not available

354

355

356

357

Table 4 Correlation analysis between bony and soft tissue structures of carpal tunnel

358

	Width of bony structures			Depth of bony structures			
		The middle of the pisiformis	The hamate hook	The proximal metacarpal bones	The middle of the pisiformis	The hamate hook	The proximal metacarpal bones
	CSA of carpal tunnel		0.769***	0.499*	0.632**	0.586**	0.764***
CSA of MN		0.365	0.362	0.051	0.519*	0.397	-0.183
Long axis of MN		0.145	0.398	0.649**	0.116	-0.166	0.434
Short axis of MN		0.268	-0.251	-0.306	0.597*	0.420	-0.275

Flattening ratio of MN	-0.147	0.361	0.628**	-0.515*	-0.461*	0.383
Swelling ratio of MN	0.263			0.232		
CAW		0.834***			0.203	
CAL		0.863***			0.273	
CAA		-0.064			-0.159	
Bowing of TCL		0.290			0.275	

359

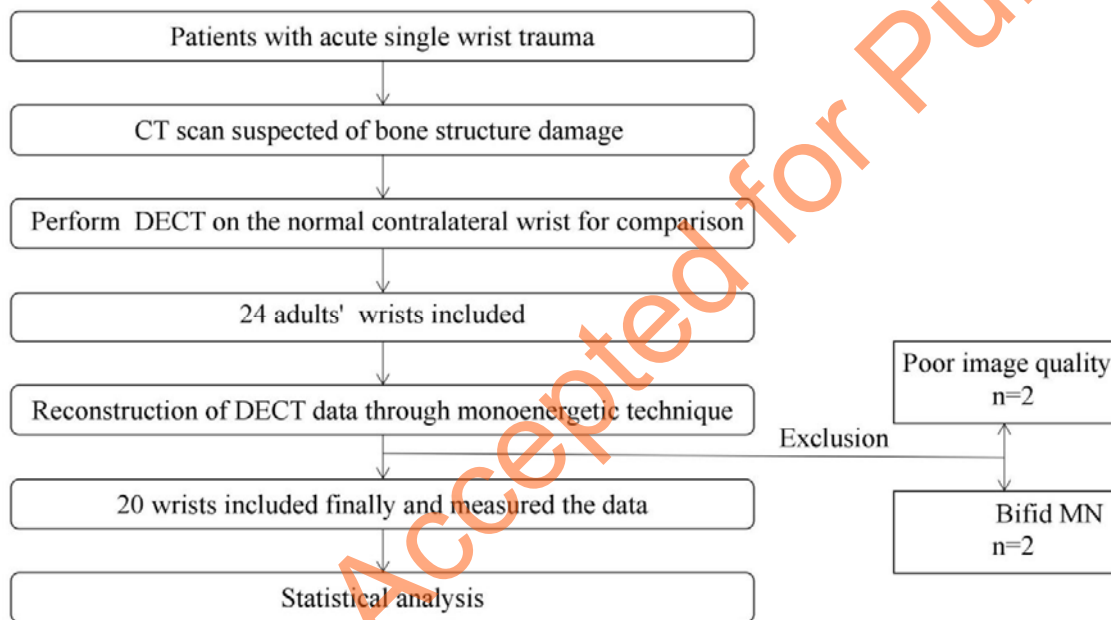
360

* $P < 0.05$, ** $P < 0.01$, *** $P < 0.001$

361

362

363



364

365

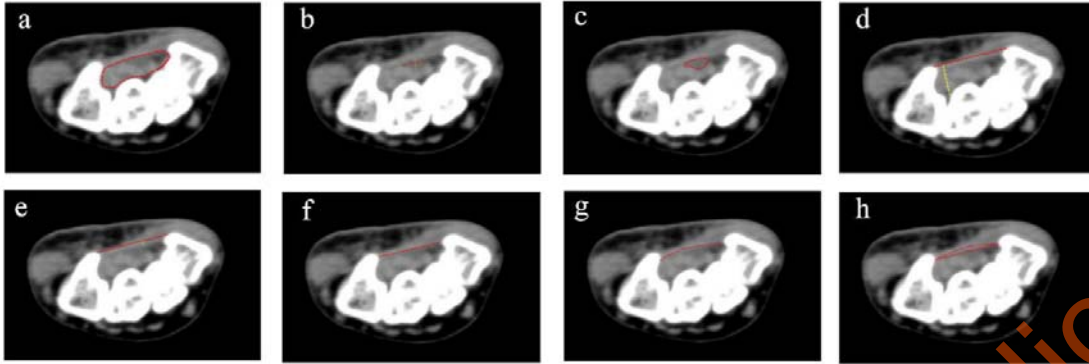
366

Fig 1: Flowchart shows inclusion and exclusion criteria for the study.

367

368

369



370

371

372

373

374

375

376

377

378

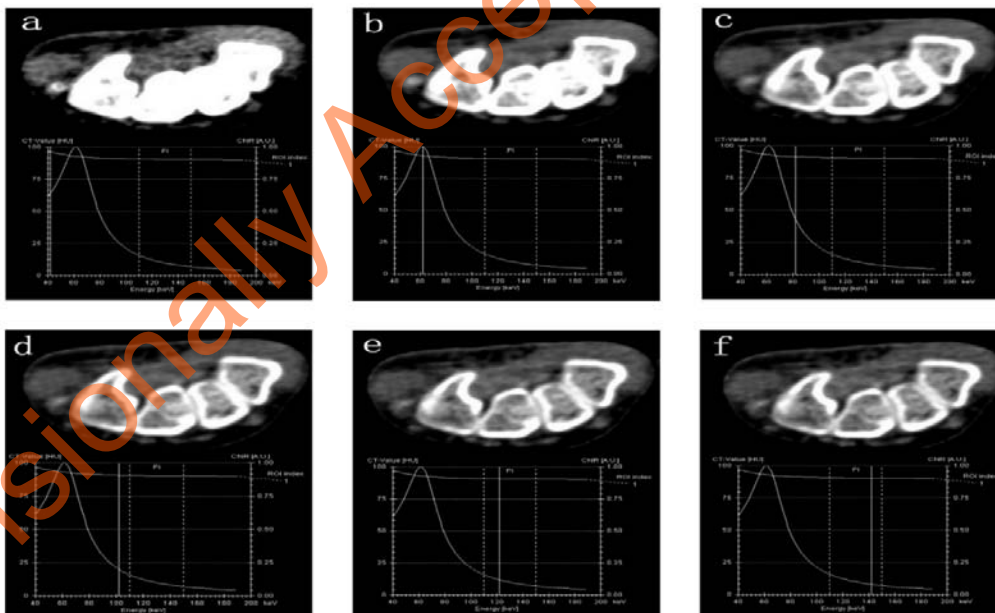
379

380

381

382

383



384

385

386

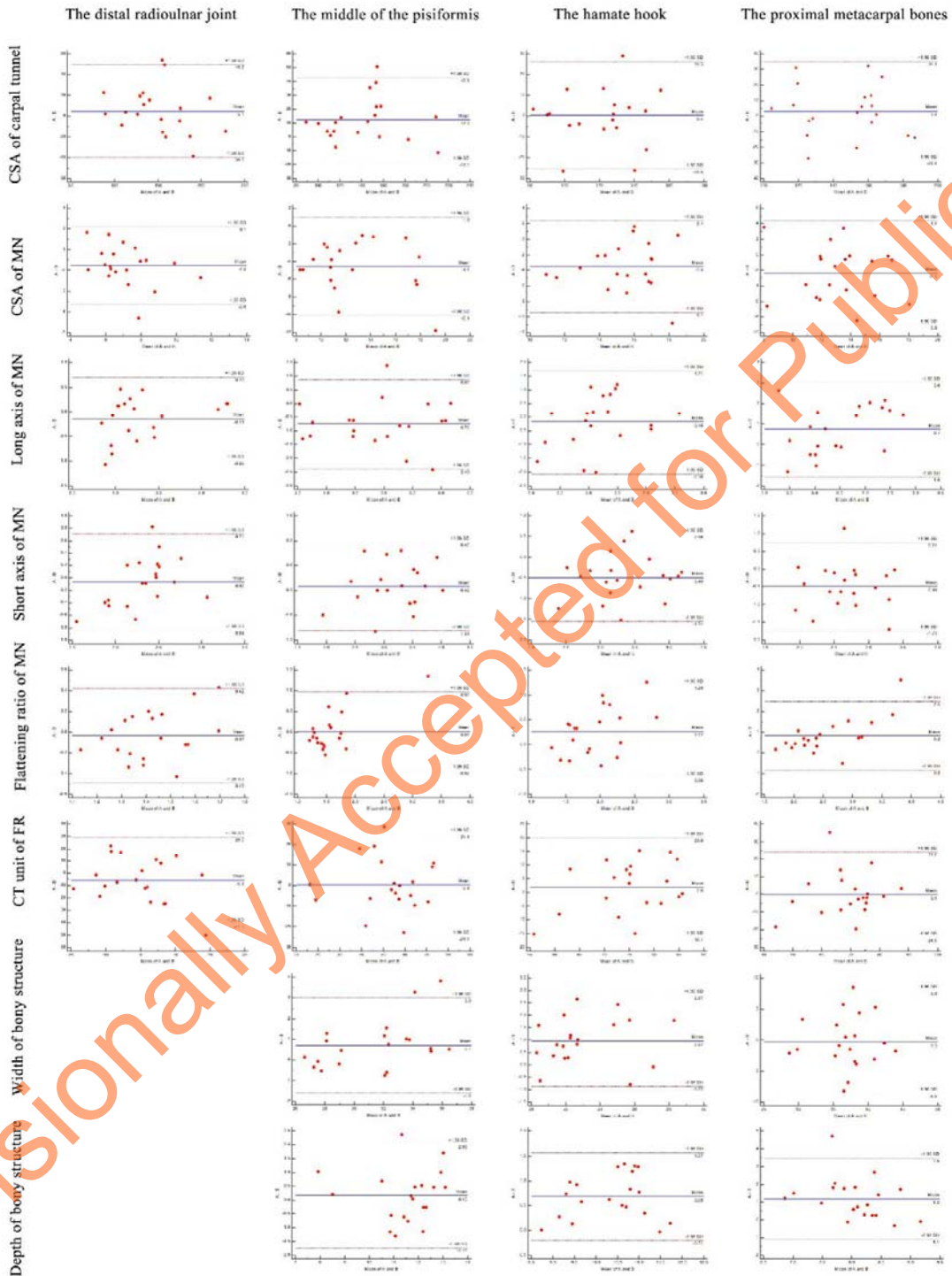
387

388

Fig 3: The images were reconstructed with 42 (a), 62 (b), 82 (c), 102 (d), 122 (e) and 142 (f) keV respectively, the best CNR through monoenergetic images was 62keV.

389

390



391

392

393

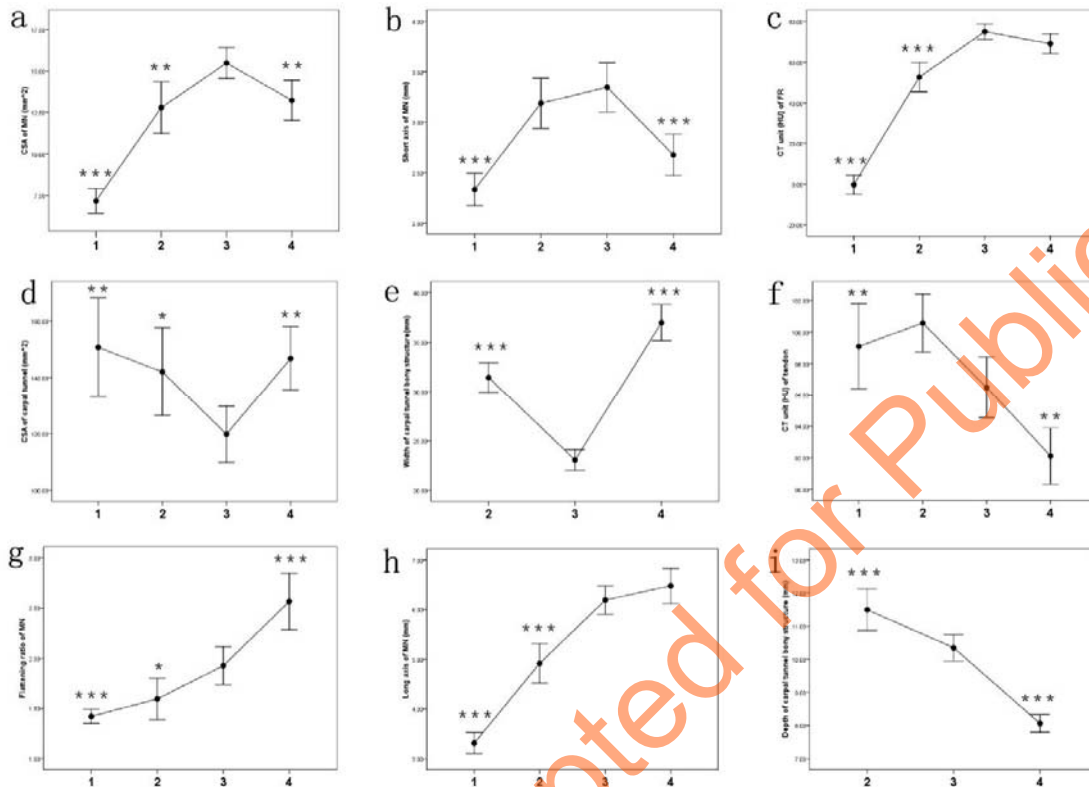
394

395

Fig 4: Bland-Altman plots demonstrated limits of agreement for carpal tunnel structures at four levels. A and B represented the two independent observer.

396

397



398

399

400

401

402

403

404

405

406

407

408

409

Fig 5: The number 1, 2, 3, 4 on the horizontal axis represented the level of the distal radioulnar joint, middle of the pisiformis, the hamate hook and the proximal metacarpal bones respectively. Anatomic tendency of CSA of MN, Short axis of MN, CT unit of ER, CSA of carpal tunnel, width of carpal tunnel bony structures, CT unit of tendon were shown in a, b, c, d, e, f respectively, we divided the above carpal tunnel structures as category 1, which resembled V-shape or inverted V-shape. g, h, i represented the anatomic tendency of flattening ratio of MN, long axis of MN, depth of carpal tunnel bony structures respectively, the above carpal tunnel structures were divided into category 2 that increased or decreased gradually.